

Mapping hidden space-charge distributions across crystalline metal oxide/group IV semiconductor interfaces

S. A. Chambers,^{1,*} M. Chrysler,² J. H. Ngai,² T.-L. Lee,³ J. Gabel[Ⓢ],³ B. E. Matthews[Ⓢ],⁴ S. R. Spurgeon,⁴ M. E. Bowden,⁵ Z. Zhu[Ⓢ],⁵ and P. V. Sushko[Ⓢ]¹

¹*Physical Sciences Division, Physical & Computational Sciences Directorate, Pacific Northwest National Laboratory, Richland, Washington 99352, USA*

²*Department of Physics, University of Texas-Arlington, Arlington, Texas 76019, USA*

³*Diamond Light Source, Ltd., Harwell Science and Innovation Campus, Didcot, Oxfordshire OX11 0DE, United Kingdom*

⁴*Nuclear Sciences Division, Energy and Environment Directorate, Pacific Northwest National Laboratory, Richland, Washington 99352, USA*

⁵*Environmental Molecular Sciences Laboratory, Earth and Biological Sciences Directorate, Pacific Northwest National Laboratory, Richland, Washington 99352, USA*



(Received 13 September 2021; revised 8 December 2021; accepted 6 January 2022; published 21 January 2022)

The electronic structures of semiconducting heterojunctions are critically dependent on composition including the presence and concentrations of dopants, both intended and unintended. Dopant profiles in the interfacial region can have major effects on band energies which in turn drive transport properties. Here we use core-level photoelectron line shapes excited with hard x rays to extract information about electric fields resulting from internal charge transfer in epitaxial $\text{La}_{0.03}\text{Sr}_{0.97}\text{Zr}_x\text{Ti}_{1-x}\text{O}_3/\text{Ge}(001)$ ($0.1 \leq x \leq 0.7$) heterostructures. Experiments were carried out for heterojunctions involving both *n*- and *p*-type Ge substrates. These heterojunctions were not amenable to electronic characterization of all regions by transport measurements because the doped substrates act as electrical shunts, precluding probing the more resistive films and masking interface conductivity. However, the core-level line shapes were found to be a rich source of information on built-in potentials that exist throughout the heterostructure, and yielded valuable insight into the impact of band bending on band alignment at the buried interfaces. The electronic effects expected for Ge with uniform *n*- and *p*-type doping are eclipsed by those of unintended oxygen dopants in the Ge near the interface. This study illustrates the power of hard x-ray photoemission spectroscopy and related modeling to determine electronic structure in material systems for which insight from traditional transport measurements is limited.

DOI: [10.1103/PhysRevMaterials.6.015002](https://doi.org/10.1103/PhysRevMaterials.6.015002)

I. INTRODUCTION

Complex metal oxide/group IV semiconductor heterojunctions are a rich test bed for discovering electronic structures that arise by forming interfaces of materials that are fundamentally different electronically, yet sufficiently similar structurally to facilitate heteroepitaxy [1–15]. Atomically well-defined interfaces of covalent semiconductors and at least partially ionic complex oxide semiconductors and insulators are expected to exhibit unique electronic structures that do not appear in homogeneous bulk environments [14,16–19]. Indeed, discovering and exploiting these properties represents a significant scientific challenge with intriguing possibilities for technological applications centered around combining the unique properties of complex oxides with those of conventional, high-mobility semiconductors. However, a major challenge in this endeavor is that of engineering the interface to gain control over the band alignment. In many device applications, leakage currents resulting from type-II or type-III band alignment preclude successful implementation of such heterostructures. For example, despite being able to improve

performance by inserting a thin buffer layer of alkaline earth oxide AEO ($AE = \text{Sr}, \text{Ba}$) [2,20], epitaxial SrTiO_3 (STO) was ultimately rejected as a gate replacement oxide for SiO_2 in Si-based CMOS technology because of leakage resulting from type-II band alignment.

The STO/Si(001) interface has been much more extensively studied than have those of other complex oxides and traditional semiconductors. Nevertheless, it is of considerable current interest to couple the dielectric, ferroelectric, and magnetic properties of complex oxides with the facile, high-mobility conductivity of semiconductors such as Ge and GaAs, in addition to Si. Ge poses some challenges not found with many other traditional semiconductors. One pertains to its small band gap, 0.66 eV. When combined with wide-gap complex oxides, the conductivity of Ge can dominate transport measurements. Indeed, the ability of Hall and resistivity measurements to distinguish contributions to electrical transport from multiple materials and interfaces conducting in parallel requires that relative conductivities of the individual components be comparable. For instance, both $\rho(T)$ vs T and Hall data for a system consisting of a single wide-gap, highly resistive material in contact with a low-gap, conductive semiconductor will be dominated by the latter and little if any information about the electronic structure of the former is

*Corresponding author: sa.chambers@pnl.gov

forthcoming. We have found this to be the case in measuring lateral transport properties for STO-based complex oxides on Ge. Because of this difficulty, it is of interest to employ an experimental technique that is equally sensitive to *all* layers in the system, independent of their individual conductivities. In principle, hard x-ray photoelectron spectroscopy (HAXPES) can yield such information over depth scales that are sufficiently large to enable multilayer systems to be probed across relevant Thomas-Fermi screening lengths.

Previously, $\text{SrZr}_x\text{Ti}_{1-x}\text{O}_3$ (SZTO) on Ge was shown to exhibit a type-I band alignment, in which the conduction band of SZTO is above that of Ge [12]. This band arrangement could potentially facilitate electron transfer from the SZTO to Ge provided the former is electron doped, analogous to modulation doping at $\text{Al}_x\text{Ga}_{1-x}\text{As}/\text{GaAs}$ heterojunctions. To explore this possibility, we utilize HAXPES and related modeling [21,22] to a family of $\text{La}_{0.03}\text{Sr}_{0.97}\text{Zr}_x\text{Ti}_{1-x}\text{O}_3/\text{Ge}(001)$ (LSZTO/Ge) heterojunctions fabricated on both *n*- and *p*-type Ge, in which La is utilized in an attempt to dope carriers into SZTO. We find, instead, that hidden sources of dopants and space charge, namely, oxygen impurities in Ge, can play a dominant role in altering band alignment and built-in fields across our LSZTO/Ge heterojunctions. Mapping built-in potentials using HAXPES enables such hidden distributions to be detected without any *a priori* knowledge or assumptions.

II. EXPERIMENT AND MODELING

Epitaxial films of $\text{La}_{0.03}\text{Sr}_{0.97}\text{Zr}_x\text{Ti}_{1-x}\text{O}_3$ (LSZTO) were grown at University of Texas at Arlington for $0.1 \leq x \leq 0.7$ on (001)-oriented, *n*- and *p*-type Ge wafers using reactive molecular beam epitaxy (MBE) in a custom-built chamber operating at a base pressure of $<3 \times 10^{-10}$ Torr. The native Ge oxide layer was removed using a wet etch process [23]. The wafers were heated to 650 °C for 5 min and a sharp (2×1) reconstruction was observed in the reflection high-energy electron diffraction (RHEED) pattern, indicating a clean, reconstructed Ge surface. A half monolayer of Sr was then deposited at 465 °C to form an oxidation resistant template for subsequent layers of LSZTO. The substrate was then cooled to room temperature at which time 2.5 monolayers (ML) of SrO and 2 ML of (Ti, Zr)O₂ were codeposited at room temperature and heated to 500 °C to form 2.5 unit cells (u.c.) of crystalline $\text{SrZr}_x\text{Ti}_{1-x}\text{O}_3$. LSZTO films of various thicknesses and compositions were subsequently grown at 580 °C by codeposition of La, Sr, Zr, and Ti in a background oxygen pressure of 4×10^{-7} Torr. Thermal effusion cells were used to evaporate La, Sr, and Ti, while Zr was evaporated using an electron-beam evaporator. All fluxes were calibrated using a quartz crystal microbalance. Typical growth rates were ~ 1 u.c. per min.

HAXPES measurements were made at the Diamond Light Source (UK) on Beamline I09. An x-ray energy of 5.9 keV was selected using a Si(111) double crystal monochromator followed by a Si(004) channel-cut high-resolution monochromator. A Scienta Omicron EW4000 high-energy hemispherical analyzer was set to a 200 eV pass energy resulting in an overall experimental resolution of ~ 250 meV, as judged by fitting a Fermi function to the Fermi edge

of a gold foil. The binding energy scale was calibrated using the Au $4f_{7/2}$ core level (CL) along with the Fermi edge of a gold foil. The films were found to be highly resistive. To avoid surface charging, we reduced the incident x-ray flux until a further fivefold reduction did not yield a measurable shift in the binding energy of the Ti $2p_{3/2}$ CL.

Angle-integrated spectra were measured with an angle of x-ray incidence of approximately 10° relative to the surface plane. The angle between the analyzer lens axis, which lies in a horizontal plane, and the incoming x rays was 93°. Thus, the photoelectron take-off angle was 13° off normal. Angle-resolved spectra were measured using an angular mode of the EW4000 analyzer. Here, the $\sim 50^\circ$ fan of acceptance was resolved by 700 pixels of a CCD camera, each $\sim 0.07^\circ$ wide, ranging in emission angles from $\sim 8^\circ$ to $\sim 58^\circ$ off normal. Spectra were then summed over 5° intervals to result in a set of ten spectra with central emission angles ranging from $\sim 10^\circ$ to $\sim 55^\circ$ off normal.

In order to extract information about the detailed dependences of the LSZTO and Ge band edges on depth, we utilize a recently developed algorithm designed to deconvolve heterojunction CL line shapes into a set of layer-resolved spectra that yields a binding energy profile for each component material in the heterostructure [22]. For many years, as-measured CL and valence-band binding energies have been utilized to determine valence-band offsets (VBOs) using the method originally developed by Kraut *et al.* [24,25]. This approach tacitly assumes that the bands are flat throughout the heterostructure. Based on this assumption, straightforward algebraic combinations of these binding energies yield experimental VBOs. Inclusion of band gaps for the component materials enables determination of the conduction band offset (CBO). However, more recent observations of asymmetric CL peak broadening have been interpreted as being due to the presence of built-in potentials and have been used to extract band-edge profiles within the different components of the heterojunction [21,22]. These band-edge profiles have in turn been found to have a substantial impact on the numerical values of the band offsets within the system, which are simply the differences between band-edge energies evaluated directly at the interface [18,26]. These observations have proliferated with the utilization of HAXPES [26,27]. Here, the larger probe depths allow more deeply buried interfaces to be interrogated across electronically relevant Debye or Thomas-Fermi screening lengths. As a result, charge-transfer phenomena across interfaces have been detected that typically do not take place when the layer thicknesses are limited to a few unit cells.

Cross-sectional scanning transmission electron microscopy (STEM) samples were prepared using a FEI Helios NanoLab Ga⁺ DualBeam Focused Ion Beam (FIB) microscope with a standard lift-out procedure. STEM high-angle annular dark field (STEM HAADF) images were collected on a probe-corrected JEOL GrandARM-300F microscope operating at 300 kV, with a convergence semiangle of 29.7 mrad and a collection angle range of 75–515 mrad. To improve signal to noise and remove scan artifacts, drift-corrected images were prepared using the SmartAlign plugin [28]; for this, a series of ten frames were collected at 512×512 px (pixels) resolution with a $2 \mu\text{s px}^{-1}$ dwell time and 90° rotations between frames. A

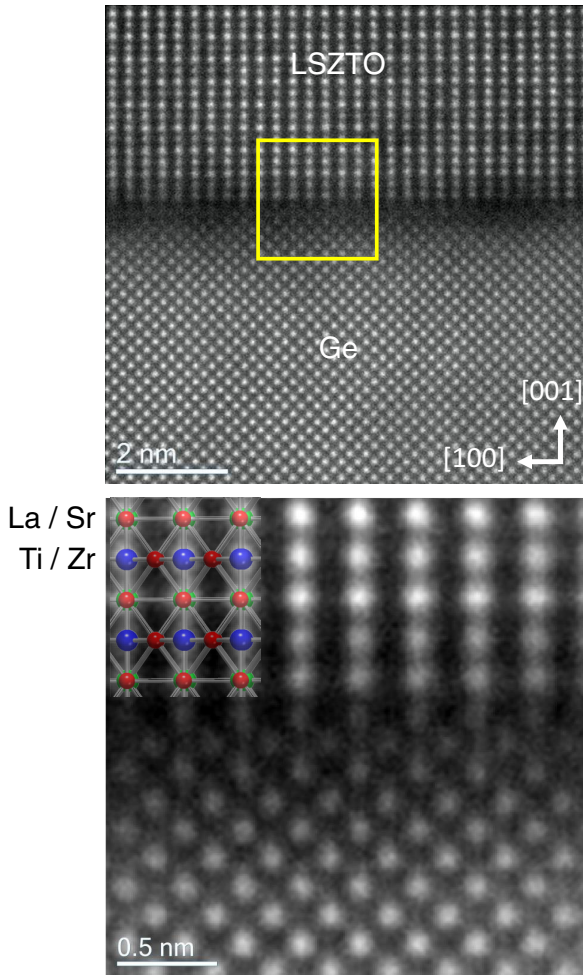


FIG. 1. Representative STEM/HAADF image for a 12 nm $\text{La}_{0.03}\text{Sr}_{0.97}\text{Zr}_{0.5}\text{Ti}_{0.5}\text{O}_3/p\text{-Ge}(001)$ heterojunction along the $[110]_{\text{LSZTO}}$ and $[010]_{\text{Ge}}$ zone axes. The lower image is a magnified version of the part of the upper image within the yellow box.

rigid alignment was then performed, followed by an average background filter to improve signal to noise for the lower image in Fig. 1.

Time of flight secondary ion mass spectrometry (ToF SIMS) measurements were performed with a TOF.SIMS5 instrument (IONTOF GmbH, Münster, Germany) using a dual beam depth profiling strategy. A 1.0 keV Cs^+ beam (~ 45 nA) was used for sputtering. The Cs^+ beam was scanned over a $300 \times 300 \mu\text{m}^2$ area. A 25.0 keV Bi_3^+ beam (~ 0.57 pA) was used as the analysis beam to collect SIMS depth profiling data. The Bi_3^+ beam was focused to be ~ 5 microns diameter and scanned over a $100 \times 100 \mu\text{m}^2$ area at the center of the Cs^+ crater.

The electrical transport characteristics of the LSZTO films on Ge could not be probed due to Ge substrate issues. We were unable to make Ohmic contacts to heterojunctions (HJs) made from $n\text{-Ge}$, possibly because of pn junction formation on the Ge side of the interface. (The formation of a p -type region near the interface due to the presence of O impurities and charge transfer to the LSZTO films is discussed in Sec. III A.) Additionally, $p\text{-Ge}$ wafers were

found to be degenerately doped at both doping concentrations used, resulting in high conductivity at all temperatures. As a result, the $p\text{-Ge}$ substrates acted as electrical shunts for the HJs, precluding measurement of interface and film properties. In order to obtain some insight, we deposited a 12 nm LSZTO film ($x = 0.5$) on the insulating oxide substrate $(\text{LaAlO}_3)_{0.3}(\text{Sr}_2\text{AlTaO}_6)_{0.7}(001)$ (LSAT). The results are shown elsewhere (see Fig. S1 in the Supplemental Material [29]). The film was highly resistive ($R_s = \sim 10^7 \Omega$ near 300 K).

Density functional theory (DFT) calculations were carried out for the stoichiometric $\text{SrZr}_{0.5}\text{Ti}_{0.5}\text{O}_3$ (SZTO)/Ge heterojunction represented using the periodic slab model. The Ge slab was 19 atomic planes thick; it was terminated with (001) planes with the lateral cell corresponding to the $\sqrt{2} \times \sqrt{2}$ bulk diamond crystallographic cell and 2×2 bulk perovskite cell. Dangling bonds on one side of the Ge slab were saturated with hydrogen atoms. The simulated SZTO film was 3 u.c. thick, terminated with a $(\text{Zr}, \text{Ti})\text{O}_2$ plane. Here we adopted the interface structure reported earlier in Ref. [30] that is consistent with the result of the STEM analysis of the samples used in this study. The lateral cell parameters of the slab supercell were fixed at the values $a = b = 8.069 \text{ \AA}$, while the off-interface parameter was fixed at 90 \AA ; this leaves a vacuum gap of well over 30 \AA . We considered four nonequivalent arrangements of Zr and Ti atoms in the SZTO film (see the Supplemental Material [29]). The total energy of each system was minimized with respect to the internal coordinates. The calculations were performed using the VASP package [31,32] and the PBESOL density functional [33]. Projector-augmented wave potentials were used to approximate the effect of the core electrons [34]. A Γ -centered $2 \times 2 \times 1$ k mesh was used for Brillouin-zone integration in the structure optimization calculations; a $8 \times 8 \times 1$ k mesh was used for calculations of the density of states (DOS). The plane-wave basis-set cutoff was set to 500 eV. The total energy convergence criterion was set to 10^{-5} eV. The charge population analysis was performed using the method developed by Bader [35,36].

III. RESULTS AND DISCUSSION

A. Electronic properties of n - and p -Ge(001) as probed with HAXPES

We have characterized our n - and p -Ge(001) substrates with their respective thin (2-3 nm) GeO_x native oxides using HAXPES. It has been previously shown that the Fermi level of clean n - and p -type Ge(001)-(2 \times 1) is pinned at the valence-band maximum (VBM) [26,37–39]. However, this is not the case when an interface to GeO_2 is formed, as seen in Fig. 2(a). The VBM (averaged over the probe depth), as estimated by extrapolating the VB leading edge to the energy axis, is ~ 0.3 – 0.5 eV below the Fermi level, with the largest value for $n\text{-Ge}$. The VB intensity from the thin native oxide falls several eV below the Fermi level owing to the much larger band gap of GeO_2 and the large valence-band offset (VBO) of the GeO_2/Ge interface [40]. As a result, the VBM is that of the underlying Ge(001). The much narrower Ge $3d$ core-level (CL) spectra for the same three Ge samples are shown in Fig. 2(b). The $3d_{5/2}$ peak energy for $n\text{-Ge}$ is

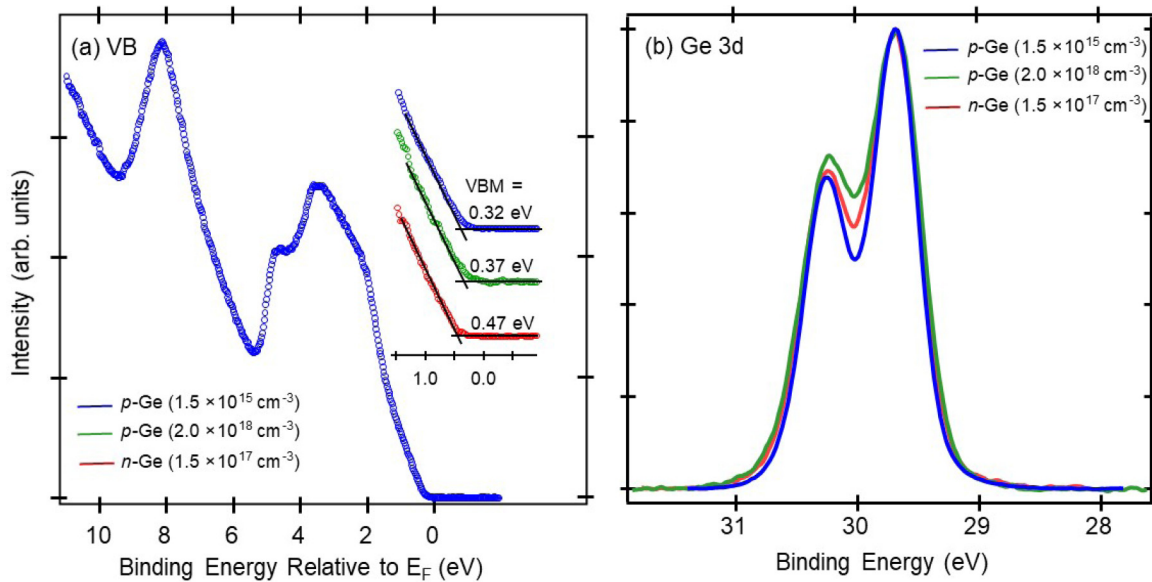


FIG. 2. Valence-band (a) and Ge 3d (b) HAXPES spectra measured at $h\nu = 6$ keV for n - and p -Ge(001) crystals with their thin native oxides. The spectrum for n -Ge has been shifted 0.22 eV to lower binding energy to overlap with the two p -Ge spectra to facilitate line shape comparison.

0.22 eV higher than those for p -Ge, which are nearly the same. The differences in VBM and CL binding energy for the three samples are presumably due to the positions of the Fermi level within the gap as well as differences in band bending and depletion width. In Fig. 2(b), the 3d spectra have been aligned to more clearly see the effect of these electronic properties on the line shapes. The overall width of this spin-orbit split doublet is expected to vary with dopant kind and quantity as the Fermi energy within the gap, the surface potential (band bending), and depletion width change.

To get an idea of what magnitude of variation can be expected from these samples, we first turn to charge neutrality considerations to estimate the expected value of the bulk Fermi energy for each sample based on its nominal dopant concentration, as supplied by the wafer vendors. For n -Ge, the Fermi energy (E_F) relative to a band edge is given by the level at which charge neutrality occurs, that is, the E_F value for which $n = N_D^+ + p$. Here n and p are the itinerant electron (hole) concentrations in the conduction (valence) bands due to thermal excitation across the gap and N_D^+ is the ionized donor concentration. Likewise, the charge neutrality condition that determines the Fermi energy for p -Ge is $p = N_A^- + n$ where n and p are defined above and N_A^- is the ionized acceptor concentration. These equations are readily solved graphically as seen in Figs. S2(a)–S2(c) in the Supplemental Material [29]; also see [41]. Combining bulk Fermi energies with the estimated surface VBM values shown in Fig. 2(a), along with depletion widths calculated using Poisson’s equation with appropriate boundary conditions, leads to the approximate energy diagrams shown in Figs. S2(d)–S2(f). This analysis suggests that the depletion width for the heavily doped p -Ge sample (see Fig. S2(e) in the Supplemental Material [29]) is rather small and comparable to the HAXPES probe depth for Ge 3d at $h\nu = 6$ keV (~ 20 nm). As a result of a ~ 0.3 V potential drop across the probe depth, the Ge 3d line shape

for this sample is expected to exhibit more broadening than that for n -Ge, for which only ~ 0.1 V is dropped across a slightly greater distance (see Fig. S2(f) in the Supplemental Material [29]). Even less broadening is expected for the lightly doped p -Ge sample for which ~ 0.1 eV is dropped across ~ 350 nm (see Fig. S2(d) in the Supplemental Material [29]). Inspection of Fig. 2(b) shows that this trend is borne out in the actual spectra. Moreover, this analysis suggests that the width of the 3d spectrum for the lightly doped p -Ge sample is not affected by band bending in any significant way and can thus be used as a basis spectrum to extract information about the built-in potential that broadens the spectrum for the heavily doped p -Ge sample. To carry this out, we have used our fitting algorithm discussed elsewhere [21,22]. The results are summarized in Fig. 3. The best fit [Fig. 3(a)] is the sum of appropriately attenuated basis spectra assigned to the top 350 atomic planes (depth = 49.4 nm) and subjected to a systematic search over binding energy ($E_{\text{Ga}3d5/2}$) space within the first 250 of these planes, with the constraint of a monotonic change in $E_{\text{Ga}3d5/2}$ with depth. The resulting family of spectra are shown as a heat plot in Fig. 3(b). Also shown in yellow is the associated VB-edge profile, $E_V(z)$, obtained using the relation $E_V(z) = E_{\text{Ga}3d5/2}(z) - 29.34$ (eV) where the offset value (29.34 eV) was determined using spectra for the low-doped p -Ge sample, for which band bending across the probe depth is negligible. Figure 3(b) reveals that the surface VBM for the heavily doped p -Ge sample is actually 0.60 eV below the Fermi level, rather than 0.37 eV as suggested by the (depth averaged) VB leading edge in Fig. 2(a). Moreover, the VBM decreases quadratically by ~ 0.32 eV in going from the surface to a depth of ~ 6 nm and then drops an additional ~ 0.05 eV to a depth of 50 nm. Within the bulk, the VBM is ~ 0.2 eV below the Fermi level, greater than expected for the nominal p -type dopant concentration. This result may result from the presence of an unintended donor impurity that can partially compensate

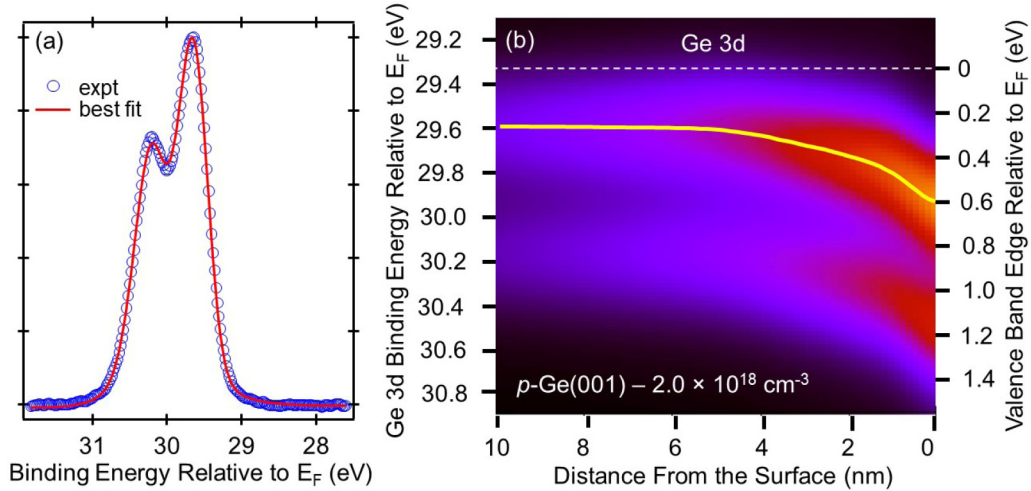


FIG. 3. (a) Fit of the Ge $3d$ spectrum for the heavily doped p -Ge(001) crystal to a sum over layers within the probe depth, using the Ge $3d$ spectrum for the lightly doped p -Ge(001) crystal, which is in a flat-band state, as the basis spectrum for each layer. (b) Heat plot showing the family of spectra which when summed together yield the best-fit spectrum in panel (a). Also shown in (b) is the valence band edge profile obtained from the Ge $3d_{5/2}$ binding energy profile (yellow curve).

the holes (such as oxygen; see discussion below), or from Ge monovacancies which have been shown by perturbed angular correlation experiments to be deep-level acceptors that fall 0.2 eV above the VBM [42].

To summarize, the difference in binding energies for n - and p -Ge (~ 0.2 eV) is smaller than one might expect because the total movement of the Fermi level across the gap in going from n type to p type must be less than the band gap, and the Ge gap is relatively low (0.66 eV). However, the built-in potential resulting from band bending affects the width of exceptionally narrow core-level features such as Ge $3d_{5/2}$ and $3d_{3/2}$ [full width at half maximum (FWHM) = ~ 0.5 eV] if it amounts to at least a few tenths of an eV across a depletion width that is comparable to the probe depth. Unfortunately, we cannot use the Ge $3d$ CL to probe the Ge side of the LSZTO/Ge interfaces because of strong overlap with Zr $4p$ (see Fig. 7). We therefore use the Ge $2p_{3/2}$ CL, an intense feature of greater width than Ge $3d_{5/2}$ which is nevertheless sufficiently sensitive to band bending to be useful.

B. Heterojunction spectra and their interpretation

A set of five heterojunctions consisting of, nominally, 12 nm films of LSZTO with different Zr mole fractions was deposited on n - and p -type Ge. We refer to these as samples (a-e) and the associated film compositions along with substrate dopant type (n or p) and dopant density are listed in

Table I. X-ray reflectivity (XRR) and STEM HAADF images indicate excellent crystallinity as well as reasonably smooth surfaces and interfaces (see Fig. S3 in the Supplemental Material [29]). Likewise, the RHEED patterns are consistent with the expected heteroepitaxial orientation, $(001)_{\text{LSZTO}}|| (001)_{\text{Ge}}$ and $[110]_{\text{LSZTO}}|| [100]_{\text{Ge}}$ (see Fig. S4 in the Supplemental Material [29]), based on lattice matching. As seen in Fig. 1 for one of the interfaces with $\text{La}_{0.03}\text{Sr}_{0.97}\text{Zr}_{0.5}\text{Ti}_{0.5}\text{O}_3$, a representative STEM HAADF image reveals a structurally coherent interface with no evidence of amorphous GeO_2 . The film is uniform and shows no sign of extended structural defects or phase separation. Since the HAADF signal is proportional to average atomic number (Z), we estimate the average signal intensity for the two sublattice planes as $Z_{A\text{ site}} = 0.03Z_{\text{La}} + 0.97Z_{\text{Sr}} = 39$ and $Z_{B\text{ site}} = 0.5Z_{\text{Zr}} + 0.5Z_{\text{Ti}} = 31$. The comparison of $Z_{A\text{ site}}$ and $Z_{B\text{ site}}$ indicates that the slightly brighter planes correspond to the A-site layers of the film, as marked by the structural diagram in Fig. 1. The target film thickness (12.0 nm) was confirmed by XRR scans and HAADF images (see Fig. S3 in the Supplemental Material [29]).

For heterostructures with as many elements as are found in the present set, overlap of CL peaks from different elements, particularly those on opposite sides of the interface, is of concern when trying to determine band-edge profiles and band alignment. To identify peak interferences, we examine the HAXPES survey spectra shown in Fig. 4. There is significant

TABLE I. Core-level binding energies along with valence-band maxima and estimated band gaps for the films in LSZTO/Ge(001) heterojunctions (all in eV).

12 nm $\text{La}_{0.03}\text{Sr}_{0.97}\text{Zr}_x\text{Ti}_{1-x}\text{O}_3/\text{Ge}(001)$	Ti $2p_{3/2}$	Sr $3d_{5/2}$	E_V	Ti $2p_{3/2}-E_V$	Sr $3d_{5/2}-E_V$	E_g
(a) $x = 0.1$, n -Ge ($1.5 \times 10^{17} \text{ cm}^{-3}$)	459.36	134.06	3.5	455.9	130.6	3.3
(b) $x = 0.3$, n -Ge ($1.5 \times 10^{17} \text{ cm}^{-3}$)	459.56	134.21	3.7	455.9	130.5	3.5
(c) $x = 0.5$, p -Ge ($1.5 \times 10^{15} \text{ cm}^{-3}$)	459.30	134.10	3.5	455.8	130.6	3.8
(d) $x = 0.5$, n -Ge ($1.5 \times 10^{17} \text{ cm}^{-3}$)	459.58	134.25	3.6	455.9	130.7	3.8
(e) $x = 0.7$, p -Ge ($2.0 \times 10^{18} \text{ cm}^{-3}$)	459.72	134.29	3.9	455.8	130.4	4.2

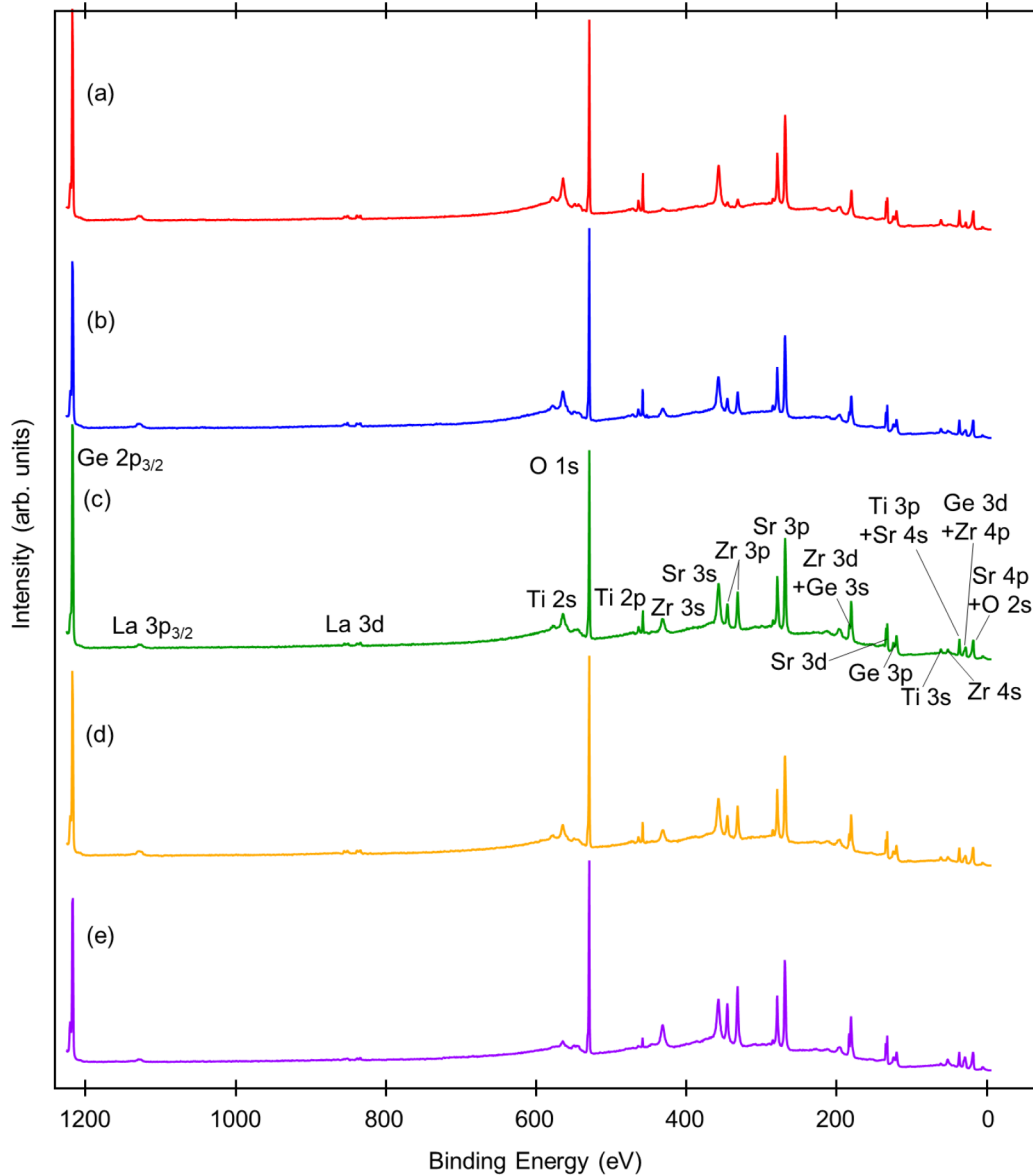


FIG. 4. Wide HAXPES scans for the set of $\text{La}_{0.03}\text{Sr}_{0.97}\text{Zr}_x\text{Ti}_{1-x}\text{O}_3/\text{Ge}(001)$ heterojunctions. The designations (a)–(e) correspond to those in Table I which gives the Zr mole fraction on the *B* sites (*x*) along with the substrate dopant type and concentration for each sample.

overlap between Ge 3*d* and Zr 4*p*, precluding the use of the former to track the band-edge energy on the Ge side of the interface. Instead, we select the Ge 2*p*_{3/2}CL as it does not interfere with any others. Likewise, there is strong overlap between Zr 3*d* and Ge 3*s* which prevents us from using Zr 3*d* to monitor band edges in the LSZTO films. Rather, we choose Ti 2*p* and Sr 3*d* which stand alone at their respective binding energies. Additionally, the integrated CL peak areas above the background were used to estimate film compositions. This analysis indicates that the stoichiometries targeted by atom beam flux measurements prior to film growth were achieved.

We now address the question of band-edge energies relative to the Fermi level (FL) in the Ge substrates and LSZTO films by analyzing the valence-band (VB) spectra, shown in Fig. 5. Previous work shows that the FL is close to the valence-band maximum (VBM) at surfaces of *n*- and *p*-Ge(001) and near in energy to the conduction band minimum (CBM) in

epitaxial STO on *p*-Ge(001) [26]. Additionally, the high band gaps of LSZTO result in the film VBM values being a few eV below the FL for the entire film set. Therefore, the leading edges of the HJ VB spectra are purely Ge 4*s*/4*p* derived and extrapolating these to the energy axis yields estimates of the VBM relative to E_F on the Ge side of the interfaces. These extrapolations lead to Ge VBM values of ~ 0.2 to ~ 0.3 eV relative to the Fermi level. To determine the VBM within the various films, we subtract an appropriately shifted and weighted Ge reference spectrum from each heterojunction spectrum, as shown at the bottom of Fig. 5 for heterojunction (c). Extrapolating the leading edge of the difference spectrum to the energy axis then yields the VBM for each film and these values, denoted as E_V , are listed in Table I. Also shown in Table I are estimated band-gap values for the LSZTO films as determined using the dependence of the band gap on the Zr mole fraction predicted by hybrid functional theory [43] in

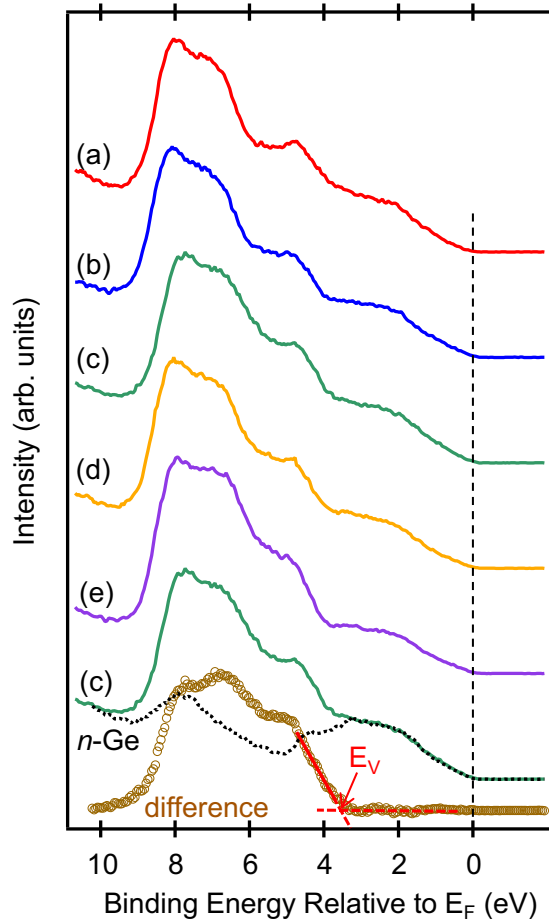


FIG. 5. Valence-band spectra for the set of $\text{La}_{0.03}\text{Sr}_{0.97}\text{Zr}_x\text{Ti}_{1-x}\text{O}_3/\text{Ge}(001)$ heterojunctions. The designations (a)–(e) correspond to those in Table I. The film spectra were isolated by subtracting an appropriately shifted and scaled Ge spectrum from each heterojunction spectrum, as shown for heterojunction (c) at the bottom. From the difference spectra, the valence-band maxima of the films (E_V) were determined by extrapolating the leading edge to the energy axis.

conjunction with the band gaps of the end members SrTiO_3 (3.25 eV) and SrZrO_3 (5.6 eV) (see Fig. S5 in the Supplemental Material [29]).

CL line shapes are key to determining the band-edge energy profiles in heterojunctions. It is important to select nonoverlapping CLs with large cross sections and relatively simple line shapes. Figure 6 shows Ti $2p$ and Sr $3d$ CL spectra for the five LSZTO films along with reference, flat-band spectra for bulk $\text{SrNb}_{0.01}\text{Ti}_{0.99}\text{O}_3(001)$. There are clear differences in the heterojunction spectra relative to those for the Nb:STO standard, and these differences carry information about built-in potentials in the heterojunctions. As a first step in the analysis, we fit the CL spectra using single Voigt functions for each spin-orbit component to determine the Ti $2p_{3/2}$ and Sr $3d_{5/2}$ peak energies. We then combine these values with the VBMs for the LSZTO(001) epitaxial films taken from Fig. 5 to yield energy differences between the CLs and the film VBM for each heterojunction, $E_{\text{CL}} - E_V$ (see Table I). Taking averages over the five heterojunctions yields values

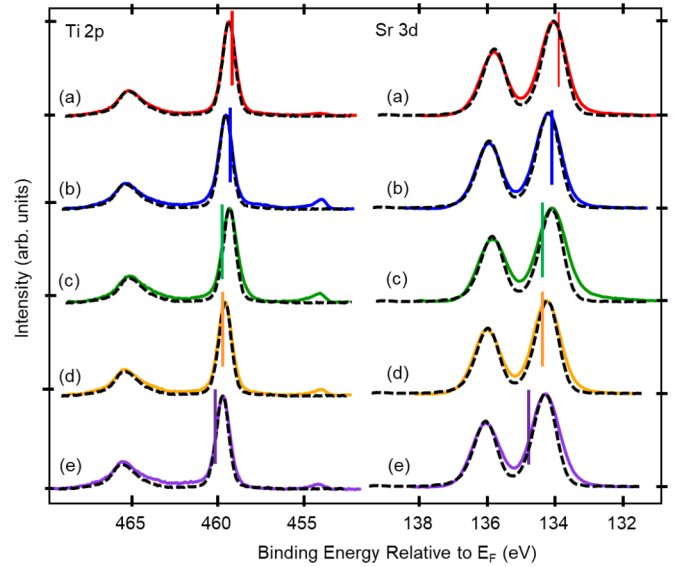


FIG. 6. Ti $2p$ and Sr $3d$ spectra for the set of $\text{La}_{0.03}\text{Sr}_{0.97}\text{Zr}_x\text{Ti}_{1-x}\text{O}_3/\text{Ge}(001)$ heterojunctions, overlapped with those for a TiO_2 -terminated $\text{SrNb}_{0.01}\text{Ti}_{0.99}\text{O}_3(001)$ single crystal (dashed). The designations (a)–(e) correspond to those in Table I. The vertical lines correspond to the Ti $2p_{3/2}$ and Sr $3d_{5/2}$ peak energies at which the Fermi level would be directly at the conduction band minimum. The fact that the Ti $2p_{3/2}$ and Sr $3d_{5/2}$ peaks are at higher binding energies for $x = 0.1$ (a) and 0.3 (b) indicates that the Fermi level is in the conduction band for these HJs. The FL then drops into the gap for $x = 0.5$ (c), (d) and 0.7 (e).

130.6(1) eV and 455.9(1) eV for Sr $3d_{5/2}$ and Ti $2p_{3/2}$, respectively, which we use throughout the rest of the analysis.

We also need a $(E_{\text{CL}} - E_V)$ value for Ge(001). After removal of the GeO_x features (Fig. S6 [29]) the Ge $2p_{3/2}$ line shapes for n - and p -type Ge(001) substrates are virtually identical, but the binding energy is ~ 0.2 eV higher for n -Ge than for p -Ge because of the different Fermi energies. The VBM for n -Ge is also ~ 0.2 eV larger than that for p -Ge. Combining VBM values from VB spectra with Ge $2p_{3/2}$ binding energies (Fig. 7), the values of $(E_{\text{Ge}2p_{3/2}} - E_V)_{\text{Ge}}$ are 1217.33(5) eV for both n - and p -Ge(001). This energy difference in turn enables determination of band offsets in the flat-band limit as well as band-edge profiles from layer-resolved CL binding energy profiles determined by carrying out a more rigorous fit of the heterojunction spectra, as described below.

Using the $(E_{\text{CL}} - E_V)$ values given above, we have placed vertical lines in Fig. 6 to indicate the Ti $2p_{3/2}$ and Sr $3d_{5/2}$ peak energies above which the Fermi level would be in the CB. The peaks are at higher binding energies than the vertical lines for $x = 0.1$ and 0.3, revealing that the FL is in the bottom portion of the CB for these HJs. In contrast, the peak is on the low binding energy side of the vertical lines for $x = 0.5$ and 0.7, indicating that the FL crosses over into the gap for $x \geq 0.5$.

The heterojunction CLs are broader than those measured for the reference bulk STO crystal for all x values. Moreover, the HJ Ti $2p_{3/2}$ spectra exhibit at least some intensity on the low binding energy side, including a feature at ~ 454.5 eV, which is close to the binding energy expected for Ti^0 [44]. A

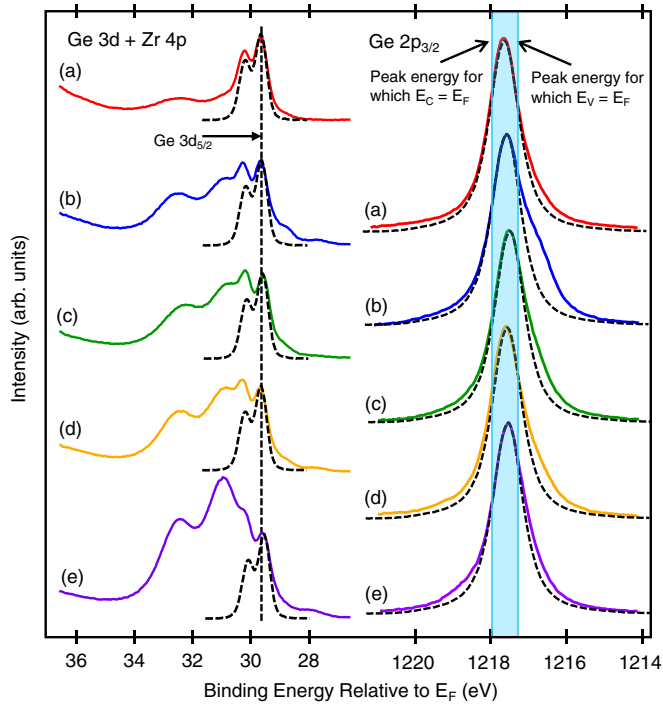


FIG. 7. Ge $3d$ and Zr $4p$ (left) along with Ge $2p_{3/2}$ (right) spectra for the family of $\text{La}_{0.03}\text{Sr}_{0.97}\text{Zr}_x\text{Ti}_{1-x}\text{O}_3/\text{Ge}(001)$ heterojunctions, overlapped with those for a n -Ge(001) bulk crystal (dashed). The designations (a–e) correspond to those in Table I. Strong overlap occurs between Ge $3d$ and Zr $4d$. However, the Ge $3d_{5/2}$ feature is fully exposed and shows a prominent knee at ~ 28.7 eV. A pronounced asymmetry is visible on the low binding energy side of the Ge $2p_{3/2}$ spectra as well. These features are due to photoemission from layers within the depletion zone created by an electric field at the interface, as explained in the text.

similar feature is visible in the Zr $3d$ spectra despite strong overlap with the Ge $3s$ (see Fig. S6 in the Supplemental Material [29]). The broadening of the Ti $2p_{3/2}$ and Sr $3d_{5/2}$ peaks is consistent with the presence of internal electric fields in the films and the low-energy features in the Ti $2p$ and Zr $3d$ spectra suggest either the presence of secondary phases containing reduced Ti and Zr metal, or strong screening of B -site Ti^{4+} and Zr^{4+} cations by trapped itinerant electrons. There is no evidence for secondary phases in any of these films or in numerous other STO, SNT0, and SZTO films deposited epitaxially on Ge and Si using the same deposition parameters. We therefore conclude that these low-energy features are due to strong screening of B -site Ti and Zr cations by La donor electrons and electrons that cross the interface from the Ge side, as discussed in detail below.

Figure 7 shows the Ge $3d/\text{Zr } 4p$ and Ge $2p_{3/2}$ regions for the HJ set. As mentioned above, we use the Ge $2p_{3/2}$ CL to monitor the Fermi level position and detect built-in potentials within the Ge substrates because strong overlap between the Ge $3d$ and the Zr $4p$ CLs precludes using the narrower Ge $3d$ for this purpose. This overlap is clearly seen on the left side of Fig. 7. Although broader than the Ge $3d$, the Ge $2p_{3/2}$ is an intense singlet with a well-defined peak energy that is straightforward to determine by spectral fitting after removal of the surface GeO_x ($x \leq 2$) features and the interfacial germanate

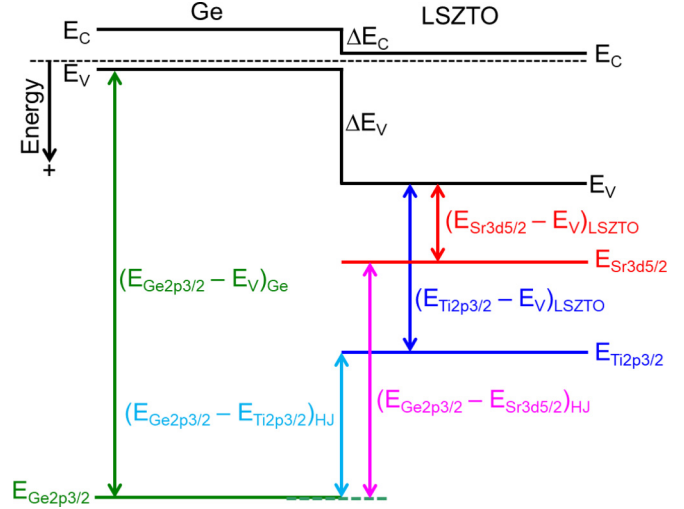


FIG. 8. Schematic diagram showing the relationship between core-level and valence-band energies as well as band offsets.

peak from the spectra from pure Ge and the HJs, respectively (see Fig. S7 in the Supplemental Material [29]). All Ge $2p_{3/2}$ peaks show clear asymmetric broadening to the low binding energy side which is also visible as an unresolved feature on the low-energy side of the Ge $3d_{5/2}$ peaks. This broadening, which is not seen in the pure Ge spectra, is consistent with the occurrence of upward band bending in the Ge. Superimposed on the Ge $2p_{3/2}$ spectra in Fig. 7 is a blue window indicating the range of peak energies for which the Fermi level would be in the Ge gap, based on the value of $(E_{\text{Ge}2p_{3/2}} - E_V)_{\text{Ge}}$. For all heterojunctions, the peak falls at or below the midgap point, consistent with the Ge VBM values estimated from the VB spectra for the HJs (Fig. 5).

The binding energies taken from the CL spectra in Figs. 6 and 7 can be used to estimate the band alignment within the flat-band approximation via the Kraut method [24,25]. Here we use two combinations of CLs to determine the VB offset (ΔE_V) and check for consistency. They are (i) Ti $2p_{3/2}$ and Ge $2p_{3/2}$ and (ii) Sr $3d_{5/2}$ and Ge $2p_{3/2}$. As seen by inspection of the schematic energy diagram in Fig. 8, the relevant formulas are

$$\Delta E_V = (E_{\text{Ge}2p_{3/2}} - E_V)_{\text{Ge}} - (E_{\text{Ti}2p_{3/2}} - E_V)_{\text{LSZTO}} - (E_{\text{Ge}2p_{3/2}} - E_{\text{Ti}2p_{3/2}})_{\text{HJ}}, \quad (1)$$

and

$$\Delta E_V = (E_{\text{Ge}2p_{3/2}} - E_V)_{\text{Ge}} - (E_{\text{Sr}3d_{5/2}} - E_V)_{\text{LSZTO}} - (E_{\text{Ge}2p_{3/2}} - E_{\text{Sr}3d_{5/2}})_{\text{HJ}}. \quad (2)$$

The CB offset (ΔE_C) is given by

$$\Delta E_C = E_g^{\text{LSZTO}} - E_g^{\text{Ge}} - \Delta E_V. \quad (3)$$

The resulting numbers are shown in Table II and the band alignments are diagrammatically illustrated in Fig. 9. All HJs exhibit a type-2 (staggered) band alignment in the flat-band approximation. The fact that the Ti $2p$ and Zr $3d$ spectra show features characteristic of strongly screened B -site cations suggests that the La donor level is hybridized with the B -site

TABLE II. Band offsets and band edges relative to the Fermi level for LSZTO/Ge(001) heterojunctions determined under the assumption of flat bands throughout (all in eV).

Heterojunction	ΔE_V (Ge 2p/Ti 2p)	ΔE_V (Ge 2p/Sr 3d)	ΔE_V (Average)	ΔE_C (Average)	E_V (Ge)	E_C (Ge)	E_V (LSZTO)	E_C (LSZTO)
(a) $x = 0.1, n$ -Ge	3.2	3.2	3.2	-0.5	0.3	-0.4	3.5	0.2
(b) $x = 0.3, n$ -Ge	3.4	3.3	3.3	-0.5	0.3	-0.4	3.7	0.2
(c) $x = 0.5, p$ -Ge	3.2	3.3	3.2	-0.2	0.2	-0.5	3.5	-0.3
(d) $x = 0.5, n$ -Ge	3.4	3.4	3.4	-0.3	0.3	-0.4	3.6	-0.2
(e) $x = 0.7, p$ -Ge	3.6	3.5	3.6	-0.1	0.2	-0.5	3.9	-0.3

cation valence orbitals. Such hybridization in turn indicates that the La donor level is near in energy to the CB minimum (CBM), which is largely Ti 3d and Zr 4d derived [43,45]. To verify this property, we performed DFT generalized gradient approximation (GGA) calculations for $\text{La}_{0.25}\text{Sr}_{0.75}\text{Zr}_x\text{Ti}_{1-x}\text{O}_3$ using PBEsol. We show the total and layer-resolved DOS elsewhere (see Fig. S8 in the Supplemental Material [29]). The La donor levels appear just below the Fermi level in all cases, with the CB DOS appearing just above the Fermi level. However, close proximity of the La donor level to the Fermi level does not result in high conductivity in LSZTO. As discussed below, the difference in Ti 3d and Zr 4d orbital energies predicted by DFT (Fig. S10 [29]) results in percolative and apparently highly resistive conduction paths.

While the flat-band approximation inherent in the Kraut method is convenient and easy to use, the broadening of the CLs is indicative of built-in potential(s) in the HJ that can strongly modify the band alignment relative to the flat-band picture. In order to explore this possibility, we select heterojunctions (c) and (d), consisting of 12 nm $\text{La}_{0.03}\text{Sr}_{0.97}\text{Zr}_{0.5}\text{Ti}_{0.5}\text{O}_3$ films grown on p -type and n -type Ge(001), respectively, to probe band-edge profiles via HAXPES fitting and analysis. Specifically, the Ge 2p_{3/2} and Sr 3d spectra were fit to sums of layer-resolved spectra to determine band-edge profiles, as described elsewhere [21,22].

We show in Figs. 10 and 11 the best fits of the HJ spectra and the associated layer-resolved CL binding energy heat maps, respectively. The excellent matches between the mea-

sured Ge 2p_{3/2} spectra and the best-fit sums over layers seen in Fig. 10 result only for physically reasonable energy profiles in which the binding energy gradients are constrained to be negative (i.e., $\partial E_{CL}/\partial z < 0$, where z is the distance from the interface with the sign convention shown in Fig. 11) [22]. The sharp drops in Ge 2p_{3/2} binding energy close to both interfaces seen in Fig. 11 are revealed in the raw spectra by the asymmetries on the lower binding energy sides (see Figs. 7 and 10). Significantly, these spectra cannot be well fit without inclusion of strong upward band bending at the interface. To verify that these asymmetries are indeed due to layers with lower binding energy close to the interface (as opposed to deeper in the bulk), we performed angle-resolved HAXPES measurements, as shown elsewhere (See Fig. S9 in the Supplemental Material [29]). Here we show the raw spectra without removal of the interfacial germanate feature because this feature is a useful marker for the interface. Both the interfacial germanate feature and the protrusion on the

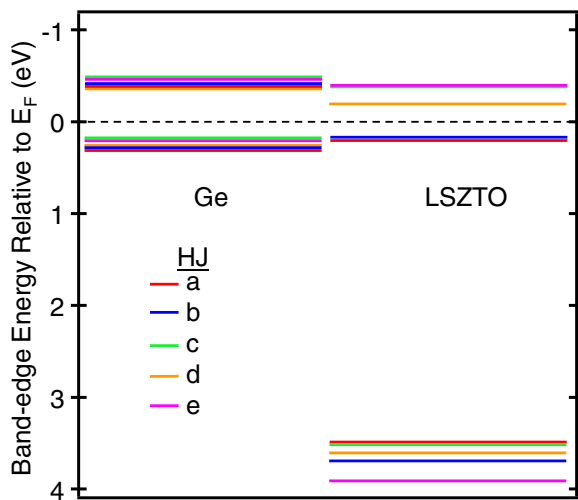


FIG. 9. Band alignments in the flat-band approximation for the family of heterojunctions, determined using Eqs. (1)–(3).

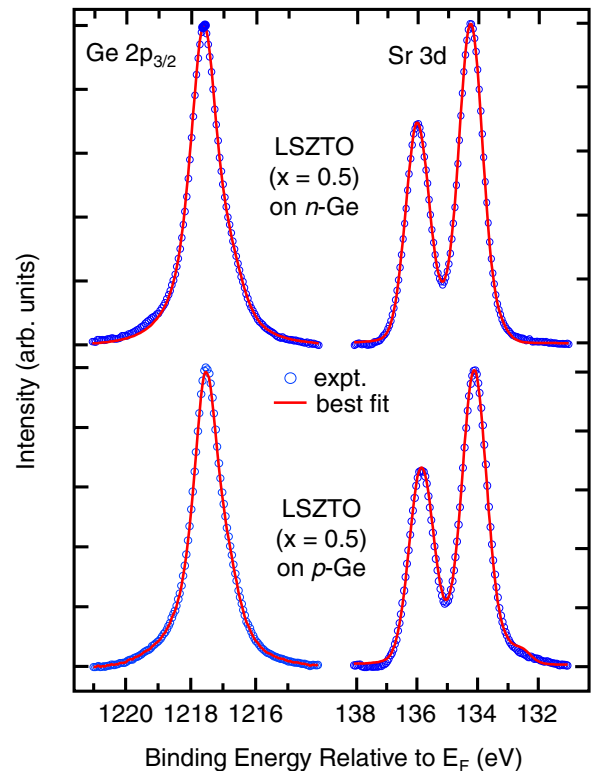


FIG. 10. Best fits of heterojunction spectra to the sums of layer-resolved, flat-band spectra shown in Fig. 11 for 12 nm $\text{La}_{0.03}\text{Sr}_{0.97}\text{Zr}_{0.5}\text{Ti}_{0.5}\text{O}_3$ on n -type and p -type Ge(001).

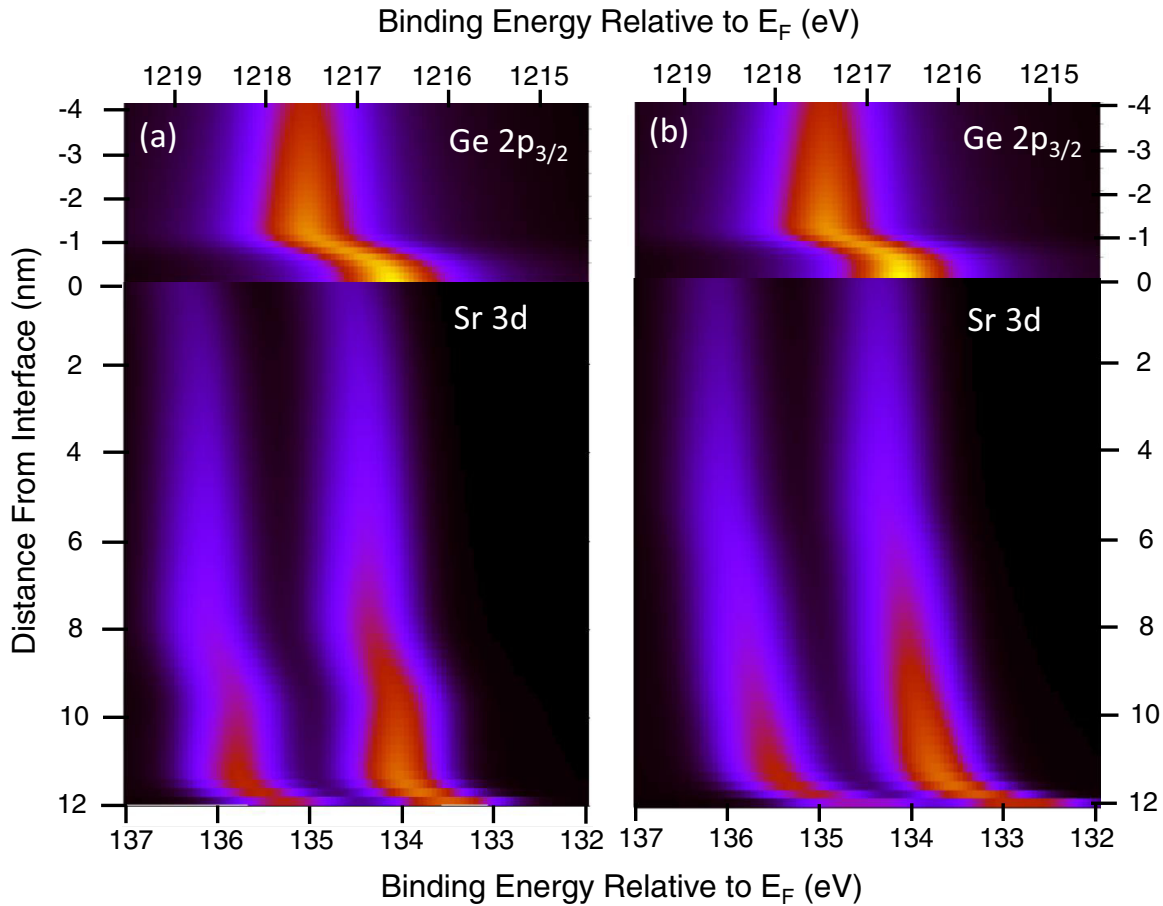


FIG. 11. Layer-resolved binding energy profiles determined by fitting Ge $2p_{3/2}$ and Sr $3d$ spectra for 12 nm $\text{La}_{0.03}\text{Sr}_{0.97}\text{Zr}_{0.5}\text{Ti}_{0.5}\text{O}_3$ on (a) n -type and (b) p -type Ge(001). Strong built-in potentials are clearly visible in both the substrates and the films, indicating charge transfer across the interface and from the interior of the film to the surface, respectively.

low binding energy side increase in intensity relative to the bulk Ge lattice peak as the photoelectron emission direction moves away from the surface normal, establishing that the protrusion does indeed originate in Ge layers close to the interface.

Surprisingly, the Ge $2p_{3/2}$ heat maps (Fig. 11) reveal sharp drops in binding energy on the Ge side of the interface for both n - and p -Ge, consistent with upward band bending for both doping types. Upward band bending is expected for HJs involving n -Ge provided electrons can readily transfer across the interface into the film. However, the built-in potential is expected to exhibit a lower gradient over a much larger depth range for the doping level used here. Likewise, downward band bending over at least ~ 15 nm is expected to occur for HJs prepared using p -Ge with the doping levels we have used. The strong upward band bending in the Ge is similar to that observed for 12 nm $\text{SrNb}_x\text{TiO}_{3-x}$ on Czochralski (CZ) and n -type Si(001) prepared similarly by MBE [18,19]. This behavior was ascribed to the presence of unintentional, ionized O donors in the near-interface Si region and subsequent electron transfer across the interface into the $\text{SrNb}_x\text{TiO}_{3-x}$. The present results suggest that electron transfer from some unintentional, ionized donor in the Ge occurs across the interface and into the LSZTO as well. The Sr $3d$ binding energies for both heterojunctions drop sharply at the surface (Fig. 11),

indicative of upward band bending at the LSZTO film surface, as also observed for the $\text{SrNb}_x\text{TiO}_{3-x}/\text{Si}(001)$ system.

The best fits for the Sr $3d$ HJ spectra (Fig. 10) are achieved by modeling the presence of antiphase domain boundaries (APBs) and stacking faults in the LSZTO films similar to those we have observed in epitaxial STO films on Ge(001) [26]. These stacking faults were in general observed to nucleate on steps at the substrate surfaces. We have assumed equal volumes of the two stacking sequences $(\text{AO})(\text{BO}_2)(\text{AO})(\text{BO}_2)\cdots$ and $(\text{BO}_2)(\text{AO})(\text{BO}_2)(\text{AO})\cdots$ from the interface in our fitting. Inspection of the Sr $3d$ heat maps (Fig. 11) reveals that the binding energies gradually decrease in going from the interface toward the surface but then drop sharply across the top nanometer of the films, again similar to what has been observed for $\text{SrNb}_x\text{TiO}_{3-x}/\text{Si}$ HJs [18].

Figure 12 shows the HJ band-edge profiles that result by subtracting $(E_{\text{Ge}2p_{3/2}} - E_V)_{\text{Ge}}$ and $(E_{\text{Sr}3d_{5/2}} - E_V)_{\text{LSZTO}}$ from the binding energy profiles for Ge $2p_{3/2}$ and Sr $3d_{5/2}$, respectively, as seen in Fig. 11. For HJs involving both n - and p -Ge substrates, the Fermi level is in the lower half of the gap well below the interface. This result is consistent with the tendency for bulk Ge to be p type as a result of Ge vacancy acceptors [42]. However, the VBM shoots sharply upward within ~ 1 nm of the interface and crosses the Fermi level and then rolls over

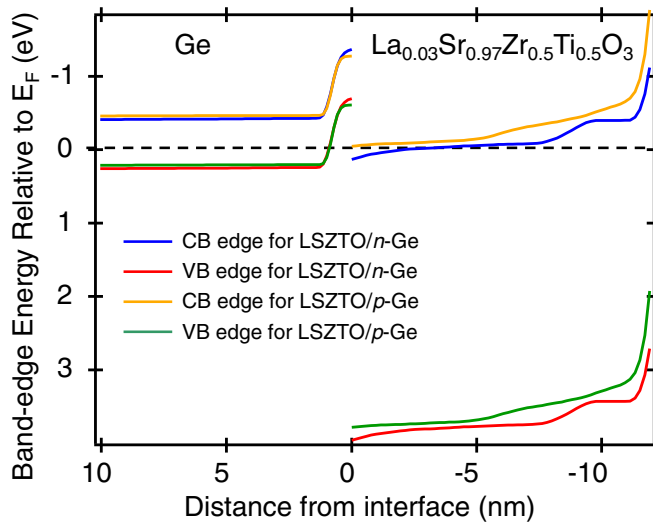


FIG. 12. Band-edge profiles extracted from binding energy profiles shown in Fig. 11 for 12 nm $\text{La}_{0.03}\text{Sr}_{0.97}\text{Zr}_{0.5}\text{Ti}_{0.5}\text{O}_3$ on n -type and p -type Ge(001) by first subtracting $(E_{\text{Ge}2p_{3/2}} - E_V)_{\text{Ge}}$ and $(E_{\text{Sr}d_{5/2}} - E_V)_{\text{LSZTO}}$ to get the VB edges, and then subtracting bulk band gaps to get the CB edges.

and flattens within the u.c. closest to the interface. The strong upward band bending in the Ge is consistent with electron transfer from Ge to LSZTO and the Ge band flattening directly at the interface is expected if a thin layer of mobile holes is present on the Ge side of the interface that would screen the electric field. The large electric field on the Ge side for both kinds of interfaces transforms the band alignment from type II (straddled) in the flat-band approximation (see discussion surrounding Fig. 9) to type III (broken) when the effects of band bending are included. The transition from type II to type III is likely driven by modulation of the interface dipole due to the presence of space charge, as recently demonstrated in the STO/Si interface [19].

The Fermi level in both $\text{La}_{0.03}\text{Sr}_{0.97}\text{Zr}_{0.5}\text{Ti}_{0.5}\text{O}_3$ films is seen to be close to the CB minimum near the interface with Ge in Fig. 12, consistent with electron transfer from the Ge. Additionally, a strong built-in potential is present near the surface of both films, resulting in sharp upward band bending. These results are consistent with surface depletion accompanying electron transfer from the interior of the LSZTO films to surface acceptors via some form of out of plane conductivity near the bottom of the CB, which is largely Ti $3d$ and Zr $4d$ derived. Our DFT calculations (Fig. S10 [29]) indicate that the Zr $4d$ projected density of states (DOS) is ~ 2 eV higher in energy than that for Ti $3d$. As a result, band transport is expected to be significantly impeded relative to that in pure La-doped STO because Zr effectively disrupts the continuous charge-transfer pathways typical of STO by introducing local potential energy barriers within the conduction band. We therefore conclude that the transport is percolative in nature, resulting in high resistivity, as measured. In this case, we expect to see evidence of Ti and Zr cation screening because of electrons trapped at the B sites; these electrons originate from La donors throughout the film as well as charge transfer across the buried interface. Indeed, angle-resolved Ti $2p_{3/2}$

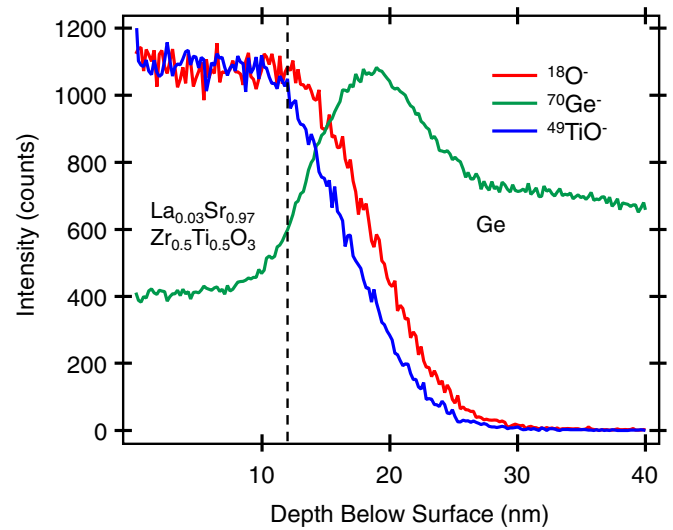


FIG. 13. ToF SIMS sputter depth profiles for $\text{La}_{0.03}\text{Sr}_{0.97}\text{Zr}_{0.5}\text{Ti}_{0.5}\text{O}_3$ on p -type Ge(001). The $^{49}\text{TiO}^-$ trace provides an upper limit for the $^{18}\text{O}^-$ knock on. The higher $^{18}\text{O}^-$ signal in the subinterface region establishes the presence of oxygen there, some of which may be thermal donors.

measurements (Fig. S11 [29]) indicate that the low-energy feature at ~ 454.5 eV in the Ti $2p_{3/2}$ spectrum is distributed across the film, reflecting the presence of carriers throughout.

The highly resistive nature of these films can be understood by the CB-edge behavior seen in Fig. 12. Strong upward band bending puts the CB minimum well above the Fermi level in the top half of each film and is expected to lead to surface depletion. Indeed, Fig. 12 constitutes the first direct electron spectroscopic evidence for surface depletion in a semiconducting complex oxide despite the detection of electrical dead layers in epitaxial films of n -SrTiO $_3$ and other oxides for decades. Lateral electron transport is further impeded by the energy mismatch between Ti $3d$ and Zr $4d$ derived DOS at the B sites and the associated effect on carrier pathways, as discussed above.

C. Unintentional doping of the Ge and its effects

The strong upward band bending in HJs made from both n - and p -Ge reveals that the effect of the original dopant profile in Ge is eclipsed by a stronger extrinsic electronic perturbation that imparts a sizable electric field across the first ~ 1 nm of the Ge. The similarity between the band-edge profiles shown in Fig. 12 and those deduced for the $\text{SrNb}_x\text{TiO}_{3-x}/\text{CZ Si}(001)$ heterojunction [18] is consistent with the unintentional donor (O) in SNTO/Si also being operative in LSZTO/Ge. Indeed, O is detected in the Ge by time of flight secondary ion mass spectrometry (ToF SIMS) as it was in Si for SNTO/Si. However, making a connection between the O atom profile detected by ToF SIMS and the built-in potential detected by HAXPES is not nearly so straightforward as it was for $\text{SrNb}_x\text{TiO}_{3-x}/\text{CZ Si}(001)$.

Figure 13 shows the depth profiles for $^{18}\text{O}^-$, $^{70}\text{Ge}^-$, and $^{49}\text{TiO}^-$ in $\text{La}_{0.03}\text{Sr}_{0.97}\text{Zr}_{0.5}\text{Ti}_{0.5}\text{O}_3/p$ -Ge(001). The TiO^- ion is included because it is very sensitive, indeed more sensitive than $^{18}\text{O}^-$, to knock-on effects in which atoms in the film

are driven into the substrate by the sputtering beam. After normalizing the signals in the LSZTO film, the $^{18}\text{O}^-$ signal is seen to be larger than that for $^{49}\text{TiO}^-$ in the subinterface region, indicating that some $^{18}\text{O}^-$ is present on the Ge side of the interface following film growth. The O may diffuse from the oxide film during film growth, or it may be present as a native impurity that concentrates near the interface during film growth. Additionally, some of the O impurities may not be electrically active. Compared to the underlying Si in the $\text{SrNb}_x\text{TiO}_{3-x}/\text{CZ-Si}$ HJs, there is a higher overall O concentration in the subinterface region of the Ge and the O profile extends to a greater depth in LSZTO/Ge.

It is well known that CZ Si contains 15–30 ppm of O as a result of crystallization in a quartz crucible. This O diffuses to and concentrates near the surface of the crystal during annealing and can be etched away to increase overall purity [46]. In our context, however, it is the O concentration gradient near the semiconductor surface that creates the interesting and unexpected electronic effects we observe for both SNT0/Si and LSZTO/Ge. It has also been known for decades that Ge crystals contain O impurities at much lower concentrations than those found in CZ Si which also act as shallow donors [47–55]. Oxygen diffusing into the melt during bulk crystal growth can occupy interstitial sites (O_i) in Ge upon solidification, resulting in the formation of Ge-O-Ge moieties that can be detected by vibrational spectroscopy if present at sufficiently high concentrations. Such impurities are electrically inactive. However, O_i species are known to convert to GeO_x clusters ($x = 1$ to 4) at temperatures in the range of 300°–500 °C, with GeO_4 being the dominant species at equilibrium. These GeO_4 clusters are electrically active and are known as thermal donors (TDs), similar to the SiO_4 TD clusters that form in Si [56]. These species are double donors with electron energy levels 0.017 and 0.037 eV below the CB minimum, as extracted from Hall data.

IV. SUMMARY

We have probed the potential energy landscape in $\text{La}_{0.03}\text{Sr}_{0.97}\text{Zr}_x\text{Ti}_{1-x}\text{O}_3/n$ - and p -Ge(001) ($0.1 \leq x \leq 0.7$) heterostructures and have detected hidden space-charge regions using hard x-ray photoelectron spectroscopy and related modeling. Unusual core-level line shapes betray the existence of built-in potentials in both the Ge substrates and the epitaxial oxide films which we extract by fitting the measured spectra to sums of layer-resolved, flat-band spectra with optimized binding energies. Angle-resolved measurements corroborate the results we obtain by fitting angle-integrated spectra and utilizing physically reasonable boundary conditions. We find evidence for electron transfer from the Ge into oxide films, as well as from the interior of the oxide films to their respective surfaces. The source of the electrons that cross the buried interfaces appears to be unintentional O donors that accumulate very near the heterojunctions.

ACKNOWLEDGMENTS

The work at Pacific Northwest National Laboratory (PNNL) was supported by the U.S. Department of Energy, Office of Science, Basic Energy Sciences under Award No. 10122 and the work at the University of Texas at Arlington was supported by the National Science Foundation (Grant No. DMR-1508530). TOF SIMS measurements and STEM sample preparation were performed at the Environmental Molecular Sciences Laboratory, a national scientific user facility sponsored by the DOE's Biological and Environmental Research program and located at PNNL. STEM imaging was performed in the Radiological Microscopy Suite (RMS), located in the Radiochemical Processing Laboratory (RPL) at PNNL. Diamond Light Source is acknowledged for time on beamline I09 under Proposal No. SI25582.

-
- [1] R. A. McKee, F. J. Walker, and M. F. Chisholm, Crystalline Oxides on Si: The First Five Monolayers, *Phys. Rev. Lett.* **81**, 3014 (1998).
- [2] R. A. McKee, F. J. Walker, and M. F. Chisholm, Physical structure and inversion charge at a semiconductor interface with a crystalline oxide, *Science* **293**, 468 (2001).
- [3] R. A. McKee, F. J. Walker, M. B. Nardelli, W. A. Shelton, and G. M. Stocks, The interface phase and the Schottky barrier for a crystalline dielectric on silicon, *Science* **300**, 1726 (2003).
- [4] H. Li, X. Hu, Y. Wei, Z. Yu, X. Zhang, R. Droopad, A. A. Demkov, J. Edwards, K. Moore, W. Ooms, J. Kulik, and P. Fejes, Two-dimensional growth of high-quality strontium titanate thin films on Si, *J. Appl. Phys.* **93**, 4521 (2003).
- [5] F. S. Aguirre-Tostado, A. Herrera-Gomez, J. C. Woicik, R. Droopad, Z. Yu, D. G. Schlom, P. Zschack, E. Karapetrova, P. Pianetta, and C. S. Hellberg, Elastic anomaly for SrTiO_3 thin films grown on Si(001), *Phys. Rev. B* **70**, 201403(R) (2004).
- [6] J. C. Woicik, H. Li, P. Zschack, E. Karapetrova, P. Ryan, C. R. Ashman, and C. S. Hellberg, Anomalous lattice expansion of coherently strained SrTiO_3 thin films grown on Si(001) by kinetically controlled sequential deposition, *Phys. Rev. B* **73**, 024112 (2006).
- [7] P. Ryan, D. Wermeille, J. W. Kim, J. C. Woicik, C. S. Hellberg, and H. Li, Domain ordering of strained 5 ML SrTiO_3 Films on Si(001), *Appl. Phys. Lett.* **90**, 221908 (2007).
- [8] J. C. Woicik, E. L. Shirley, C. S. Hellberg, K. E. Andersen, S. Sambasivan, D. A. Fischer, B. D. Chapman, E. A. Stern, P. Ryan, D. L. Ederer, and H. Li, Ferroelectric distortion in SrTiO_3 thin films on Si(001) by x-ray absorption fine structure spectroscopy: Experiment and first-principles calculations, *Phys. Rev. B* **75**, 140103(R) (2007).
- [9] M. P. Warusawithana, C. Cen, C. R. Sleasman, J. C. Woicik, Y. L. Li, L. F. Kourkoutis, J. A. Klug, H. Li, P. Ryan, L. P. Wang, M. Bedzyk, D. A. Muller, L. Q. Chen, J. Levy, and D. G. Schlom, A ferroelectric oxide made directly on silicon, *Science* **324**, 367 (2009).
- [10] A. A. Demkov and A. B. Posadas, *Integration of Functional Oxides with Semiconductors* (Springer-Verlag, New York, 2014).

- [11] J. H. Ngai, D. P. Kumah, C. H. Ahn, and F. J. Walker, Hysteretic electrical transport in $\text{BaTiO}_3/\text{Ba}_{1-x}\text{Sr}_x\text{TiO}_3/\text{Ge}$ heterostructures, *Appl. Phys. Lett.* **104**, 062905 (2014).
- [12] M. Jahangir-Moghadam, K. Ahmadi-Majlan, X. Shen, T. Droubay, M. Bowden, M. Chrysler, D. Su, S. A. Chambers, and J. H. Ngai, Band-gap engineering at a semiconductor-crystalline oxide interface, *Adv. Mater. Int.* **2**, 1400497 (2015).
- [13] Z. H. Lim, K. Ahmadi-Majlan, E. D. Grimley, Y. Du, M. Bowden, R. Moghadam, J. M. LeBeau, S. A. Chambers, and J. H. Ngai, Structural and electrical properties of single crystalline SrZrO_3 epitaxially grown on Ge (001), *J. Appl. Phys.* **122**, 084102 (2017).
- [14] J. H. Ngai, K. Ahmadi-Majlan, J. Moghadam, M. Chrysler, D. Kumah, F. J. Walker, C. H. Ahn, T. Droubay, Y. Du, S. A. Chambers, M. Bowden, X. Shen, and D. Su, Electrically coupling complex oxides to semiconductors: A route to novel material functionalities, *J. Mater. Res.* **32**, 249 (2017).
- [15] P. Laukkanen and M. Kuzmin, in *Advanced Nanomaterials for Solar Cells and Light Emitting Diodes*, edited by F. Gao (Elsevier, Amsterdam, 2019), p. 423.
- [16] L. Ji, M. D. McDaniel, S. J. Wang, A. B. Posadas, X. H. Li, H. Y. Huang, J. C. Lee, A. A. Demkov, A. J. Bard, J. G. Ekerdt, and E. T. Yu, A silicon-based photocathode for water reduction with an epitaxial SrTiO_3 protection layer and a nanostructured catalyst, *Nat. Nanotechnol.* **10**, 84 (2015).
- [17] L. Kornblum, D. P. Fenning, J. Faucher, J. Hwang, A. Boni, M. G. Han, M. D. Morales-Acosta, Y. Zhu, E. I. Altman, M. L. Lee, C. H. Ahn, F. J. Walker, and Y. Shao-Horn, Solar hydrogen production using epitaxial SrTiO_3 on a GaAs Photovoltaic, *Energy Environ. Sci.* **10**, 377 (2016).
- [18] Z. H. Lim, N. F. Quackenbush, A. N. Penn, M. Chrysler, M. Bowden, Z. Zhu, J. M. Ablett, T.-L. Lee, J. M. LeBeau, J. C. Woicik, P. V. Sushko, S. A. Chambers, and J. H. Ngai, Charge Transfer and Built-in Electric Fields between a Crystalline Oxide and Silicon, *Phys. Rev. Lett.* **123**, 026805 (2019).
- [19] M. Chrysler, J. Gabel, T.-L. Lee, A. N. Penn, B. E. Matthews, D. M. Kepaptsoglou, Q. M. Ramasse, J. R. Paudel, R. K. Sah, J. D. Grassi, Z. Zhu, A. X. Gray, J. M. LeBeau, S. R. Spurgeon, S. A. Chambers, P. V. Sushko, and J. H. Ngai, Tuning band alignment at a semiconductor-crystalline oxide heterojunction via electrostatic modulation of the interfacial dipole, *Phys. Rev. Mater.* **5**, 104603 (2021).
- [20] S. Jeon, F. J. Walker, C. A. Billman, R. A. McKee, and H. Hwang, Electrical characteristics of epitaxially grown SrTiO_3 on silicon for metal-insulator-semiconductor gate dielectric applications, *IEEE Electron Device Lett.* **24**, 218 (2003).
- [21] S. A. Chambers and P. V. Sushko, Probing energy landscapes in multilayer heterostructures: Challenges and opportunities, *APL Mater.* **7**, 110904 (2019).
- [22] P. V. Sushko and S. A. Chambers, Extracting band edge profiles at semiconductor heterostructures from hard-x-ray core-level photoelectron spectra, *Sci. Rep.* **10**, 13028 (2020).
- [23] P. Ponath, A. B. Posadas, R. C. Hatch, and A. A. Demkov, Preparation of a clean Ge(001) surface using oxygen plasma cleaning, *J. Vac. Sci. Technol. B* **31**, 031201 (2013).
- [24] E. A. Kraut, R. W. Grant, J. R. Waldrop, and S. P. Kowalczyk, Precise Determination of the Valence-Band Edge in X-Ray Photoemission Spectra: Application to Measurement of Semiconductor Interface Potentials, *Phys. Rev. Lett.* **44**, 1620 (1980).
- [25] E. A. Kraut, R. W. Grant, J. R. Waldrop, and S. P. Kowalczyk, Semiconductor core-level to valence-band maximum binding-energy differences: Precise determination by x-ray photoelectron-spectroscopy, *Phys. Rev. B* **28**, 1965 (1983).
- [26] Y. Du, P. V. Sushko, S. R. Spurgeon, M. E. Bowden, J. M. Ablett, T.-L. Lee, N. F. Quackenbush, J. C. Woicik, and S. A. Chambers, Layer-resolved band bending at the $n\text{-SrTiO}_3(001)/p\text{-Ge}(001)$ interface, *Phys. Rev. Mater.* **2**, 094602 (2018).
- [27] S. A. Chambers, Y. Du, R. B. Comes, S. R. Spurgeon, and P. V. Sushko, The effects of core-level broadening in determining band alignment at the epitaxial $\text{SrTiO}_3(001)/p\text{-Ge}(001)$ heterojunction, *Appl. Phys. Lett.* **110**, 082104 (2017).
- [28] L. Jones, H. Yang, T. J. Pennycook, M. S. J. Marshall, S. Van Aert, N. D. Browning, M. R. Castell, and P. D. Nellist, Smart Align—a new tool for robust non-rigid registration of scanning microscope Data, *Adv. Struct. Chem. Imaging* **1**, 8 (2015).
- [29] See Supplemental Material at <http://link.aps.org/supplemental/10.1103/PhysRevMaterials.6.015002> for charge neutrality calculations for Ge, transport data, x-ray reflectivity and reflection high-energy electron diffraction results, calculated band gaps for solid solutions, additional hard x-ray photoemission spectra, and *ab initio* modeling.
- [30] A. M. Kolpak and S. Ismail-Beigi, Interface structure and film polarization in epitaxial $\text{SrTiO}_3/\text{Si}(001)$, *Phys. Rev. B* **85**, 195318 (2012).
- [31] G. Kresse and J. Hafner, *Ab initio* molecular-dynamics simulation of the liquid-metal–amorphous-semiconductor transition in germanium, *Phys. Rev. B* **49**, 14251 (1994).
- [32] G. Kresse and J. Furthmüller, Efficient iterative schemes for *ab initio* total-energy calculations using a plane-wave basis set, *Phys. Rev. B* **54**, 11169 (1996).
- [33] J. P. Perdew, K. Burke, and M. Ernzerhof, Generalized Gradient Approximation Made Simple, *Phys. Rev. Lett.* **77**, 3865 (1996).
- [34] P. E. Blochl, Projector augmented-wave method, *Phys. Rev. B* **50**, 17953 (1994).
- [35] R. F. W. Bader, *Atoms in Molecules: A Quantum Theory* (Oxford University Press, Oxford, 1990).
- [36] W. Tang, E. Sanville, and G. Henkelman, A grid-based Bader analysis algorithm without lattice bias, *J. Phys.: Condens. Matter* **21**, 084204 (2009).
- [37] E. Landemark, C. J. Karlsson, L. S. O. Johansson, and R. I. G. Uhrberg, Electronic structure of clean and hydrogen-chemisorbed Ge(001) surfaces studied by photoelectron spectroscopy, *Phys. Rev. B* **49**, 16523 (1994).
- [38] M. Wojtaszek, J. Lis, R. Zuzak, B. Such, and M. Szymonski, Inversion layer on the Ge(001) surface from the four-probe conductance measurements, *Appl. Phys. Lett.* **105**, 042111 (2014).
- [39] M. Wojtaszek, R. Zuzak, S. Godlewski, M. Kolmer, J. Lis, B. Such, and M. Szymonski, Fermi level pinning at the Ge(001) surface—a case for non-standard explanation, *J. Appl. Phys.* **118**, 185703 (2015).
- [40] M. Yang, R. Q. Wu, Q. Chen, W. S. Deng, Y. P. Feng, J. W. Chai, J. S. Pan, and S. J. Wang, Impact of oxide defects on band offset at GeO_2/Ge interface, *Appl. Phys. Lett.* **94**, 142903 (2009).

- [41] S. M. Sze, *Physics of Semiconductor Devices* (John Wiley and Sons, New York, 2007).
- [42] H. Haesslein, R. Sielemann, and C. Zistl, Vacancies and Self-Interstitials in Germanium Observed by Perturbed Angular Correlation Spectroscopy, *Phys. Rev. Lett.* **80**, 2626 (1998).
- [43] L. Weston, A. Janotti, X. Y. Cui, B. Himmetoglu, C. Stampfl, and C. G. Van de Walle, Structural and electronic properties of SrZrO₃ and Sr(Ti, Zr)O₃ alloys, *Phys. Rev. B* **92**, 085201 (2015).
- [44] J. F. Moulder, W. F. Stickle, P. E. Sobol, and K. D. Bomben, *Handbook of X-Ray Photoelectron Spectroscopy* (Perkin-Elmer Corporation, Eden Prairie, MN, 1992).
- [45] G. Celik and S. Cabuk, First-principles study of electronic structure and optical properties of Sr(Ti, Zr)O₃, *Cent. Eur. J. Phys.* **11**, 387 (2013).
- [46] R. C. Newman, Oxygen diffusion and precipitation in Czochralski silicon, *J. Phys.: Condens. Matter* **12**, R335 (2000) .
- [47] G. Elliott, Oxygen as a donor element in germanium, *Nature (London)* **180**, 1350 (1957).
- [48] J. Bloem, C. Haas, and P. Penning, Properties of oxygen in germanium, *J. Phys. Chem. Solids* **12**, 22 (1959).
- [49] C. S. Fuller, W. Kaiser, and C. D. Thurmond, Donor equilibria in the germanium-oxygen system, *J. Phys. Chem. Solids* **17**, 301 (1961).
- [50] W. Kaiser and C. D. Thurmond, Solubility of oxygen in germanium, *J. Appl. Phys.* **32**, 115 (1961).
- [51] W. Kaiser, Electrical and optical investigations of donor formation in oxygen-doped germanium, *J. Phys. Chem. Solids* **23**, 255 (1962).
- [52] C. S. Fuller and F. H. Doleiden, The ionization behavior of donors formed from oxygen in germanium, *J. Phys. Chem. Solids* **19**, 251 (1961).
- [53] C. S. Fuller, Kinetics of donor reactions in oxygen-doped germanium, *J. Phys. Chem. Solids* **19**, 18 (1961).
- [54] V. M. Babich, P. I. Baranskii, and V. A. Shershel, Influence of oxygen and impurity-oxygen complexes on magnetoresistance of *n*-Ge in strong magnetic fields, *Phys. Status Solidi* **42**, K23 (1970).
- [55] P. Clauws, Oxygen related defects in germanium, *Mater. Sci. Eng.: B* **36**, 213 (1996).
- [56] W. Kaiser, H. L. Frisch, and H. Reiss, Mechanism of the formation of donor states in heat-treated silicon, *Phys. Rev.* **112**, 1546 (1958).